J. Fluid Mech. (1990), *vol.* 213, *pp.* 397–418
Printed in Great Britain

Liquid metal flow through a sharp elbow in the plane of a strong magnetic field

By T. J. MOON[1] AND J. S. WALKER[2]

[1] Mechanical Engineering Department, The University of Texas at Austin, Austin, TX 78712-1063, USA

[2] Department of Mechanical and Industrial Engineering, University of Illinois, Urbana, IL 61801, USA

(Received 15 February 1989)

This paper treats a liquid-metal flow through a sharp elbow connecting two constant-area, rectangular ducts with thin metal walls. There is a uniform, strong magnetic field in the plane of the centrelines of the ducts. An analytical solution with a series of eigenfunctions is possible for two sectors of the geometry, while a finite-difference relaxation solution is used for the third sector. The analytical and numerical solutions are coupled at the common boundaries by a combination of a Galerkin minimization of a residual and of integrals of the basic conservation laws over cells adjacent to each boundary. Results are presented for the three-dimensional pressure, electric potential function and fluid velocity. The pressure drop due to the three-dimensional effects near the elbow is also presented. The eigenfunction series represents a quite general solution for any three-dimensional flow in a rectangular duct with a skewed magnetic field.

1. Introduction

A large pressure drop may be required to pump a liquid metal through a duct in the presence of a strong magnetic field because of the large electromagnetic (EM) body force opposing the flow. A large pressure drop may imply an undesirably large pumping power or undesirably large stresses in the walls confining the flow. The fluid motion across the magnetic field drives an electric current in the liquid metal, and the electric current produces the EM body force opposing the motion. If the inside surfaces of the duct walls are electrically insulated, then the electric current path is completed through the thin Hartmann layers adjacent to the walls. These thin layers have a large electrical resistance, so that the electric current and pressure drop are small. However, many liquid metals are not compatible with electrically insulating materials, particularly at elevated temperatures, so that uninsulated metal walls must be used. When the electric current path is completed through the low-resistance metal walls, the current and pressure drop are much larger. Thin metal walls have a higher resistance than thick ones and thus reduce the pressure drop, but the wall thickness is frequently restricted by structural requirements.

If the direction of the flow or of the magnetic field can be changed, then the pressure drop can be reduced because the pressure gradient for fully developed flow is proportional to the square of the magnetic field component which is perpendicular to the direction of the flow. For a liquid-lithium coolant flow inside a magnetic-confinement fusion reactor, Hoffman & Carlson (1971) propose the alignment of the ducts with the magnetic field lines, so that the pressure gradient is reduced to that

for laminar ordinary hydrodynamic (OHD) flow. If the angle between the duct's centreline and the local magnetic field is α, the wall conductance ratio for the metal walls is c and the Hartmann number is M, then the ratio of the pressure gradient for fully developed MHD flow to that for OHD flow is comparable to $cM^2\sin^2\alpha$. For fusion reactor lithium coolant flows, typical values of c and M are 0.01 and 10^4, respectively. Therefore, the MHD pressure gradient is only less than the OHD one for $\alpha < 0.06°$. In a real design, such a perfect alignment would be difficult to achieve. Achieving alignments within, say, 5° would be a more practical design goal. For $\alpha = 5°$, the MHD pressure gradient is roughly 10^4 times the laminar OHD one, but is 0.01 times the MHD pressure gradient for $\alpha = 90°$.

Several recent designs for the liquid-lithium cooling systems in Tokamaks have reduced the overall pressure drop by making all high-velocity flows nearly parallel to the magnetic field lines (Malang *et al.* 1988; Smith *et al.* 1985). A Tokamak is a magnetic-confinement fusion reactor with a toroidal geometry. In the region of the liquid-lithium flow, there is a toroidal magnetic field B_T due to the magnet coils around the torus and a poloidal magnetic field B_P due to the electric current in the plasma. Here, the toroidal and poloidal directions are around the large and small circumferences of the torus, respectively. In a typical design, $B_P = 0.1B_T$, so that a liquid-lithium flow in the toroidal direction is nearly parallel to the magnetic field lines, while a flow in the poloidal direction is nearly perpendicular to the field lines. Coolant flows in the toroidal direction completely around the large circumference of the torus would minimize the pressure drop, but maintenance requirements dictate that the reactor be composed of a large number of independent, wedge-shaped segments which can be removed through the space between two adjacent magnet coils.

In the design for the blanket comparison and selection study (Smith *et al.* 1985), the coolant ducts close to the plasma are short, toroidal ducts with a large liquid-metal velocity. A large coolant velocity is necessary close to the plasma because the energy deposition rate is large here. The pressure drop is acceptable in spite of the large velocity because the ducts are nearly parallel to the magnetic field. Further from the plasma, there are large poloidal ducts which feed cooler liquid to the toroidal ducts and carry hotter liquid away from them. The velocity in these poloidal ducts can be much smaller because the energy deposition here is very small, so that the pressure drop is acceptable in spite of the large transverse magnetic field component for poloidal ducts. At the end of the blanket comparison and selection study, important questions about the three-dimensional flow near the junction of a poloidal and toroidal duct remained unanswered and appeared to be critical for the feasibility of this and similar designs. In particular, there was no reliable estimate of the extra pressure drop associated with the sharp elbow between two ducts, one nearly parallel and the other nearly perpendicular to the magnetic field, and there was no reliable prediction of the three-dimensional flow distribution in a region with a high energy deposition rate.

The present analysis captures the essential physics of the junction of a poloidal duct and a toroidal duct in a Tokamak coolant system in the context of a basic problem in liquid-metal magnetohydrodynamics with relevance to other technological applications. We treat the flow in a sharp elbow composed of two semi-infinite, constant-area, rectangular ducts with one end bevelled at 45° and joined to form a 90° mitre corner. There is a uniform magnetic field in the plane of the centrelines of the two ducts. The analysis applies for any angle between the magnetic field direction and the duct centrelines. However, results are only presented for a

magnetic field at angles of 84.29° and 5.71° to the centrelines of the upstream and downstream ducts, corresponding to the poloidal and toroidal ducts, respectively, with $B_P = 0.1B_T$. For a strong magnetic field, inertial effects are negligible so that solution applies as well for flow in the opposite direction.

Hunt & Holroyd (1977) present a qualitative discussion of the flow in an elbow in the plane of a uniform magnetic field. Their discussion is based on the asymptotic solutions for flows in non-uniform magnetic fields presented by Holroyd & Walker (1978). Hunt & Holroyd conclude that the flow becomes concentrated into jets with a large region of stagnant liquid, as one duct approaches alignment with the magnetic field. Subsequently, Hunt developed an order-of-magnitude estimate for a sharp elbow with a perfect alignment for one duct (cited by Holroyd 1980). Hunt concludes that the flow in the aligned duct is confined to a thin region with $O(N^{-\frac{1}{3}})$ dimensionless thickness, where N is the interaction parameter which is typically 10^4–10^5 for a fusion reactor cooling system. The fluid outside this thin region is stagnant. The flow region spreads very slowly across the cross-section of the aligned duct as we move away from the elbow, so that the velocity outside this region remains small for a long distance. The pressure drop predicted from Hunt's order-of-magnitude estimate (Holroyd 1980) is acceptable for the Tokamak cooling system (Holroyd & Mitchell 1982; Smith *et al.* 1985), but the flow pattern would be unacceptable for the local heat transfer. If the flow from the poloidal duct does not fill the toroidal duct and there is stagnant liquid near the plasma, then the local temperature would become unacceptably high. The discussion of Hunt & Holroyd (1977) and Hunt's order-of-magnitude estimate are both based on the asymptotic solutions of Holroyd & Walker (1978) for $c \ll 1$, where c is the wall conductance ratio which is typically 0.01–0.1 for fusion reactor lithium cooling systems.

Recent experiments at Argonne National Laboratory have indicated that an asymptotic analysis for $c \ll 1$ is not appropriate for fusion reactor cooling systems with $c = 0.01$–0.1 (Picologlou *et al.* 1986). Reflection upon the analysis of Holroyd & Walker (1978) reveals that it assumes that $\lambda_1 c^{\frac{1}{2}} \ll 1$, where λ_1 is an eigenvalue which is 10.6 for the circular pipes treated by Holroyd & Walker. Even for $c = 0.01$, $\lambda_1 c^{\frac{1}{2}}$ is greater than one, so that the asymptotic analysis does not apply. In particular, the asymptotic analysis predicts three-dimensional flow concentrations in small fractions of the duct's cross-section, with large regions of stagnent liquid, while real flows with $c = 0.01$ do not involve such severe flow distributions (Reed *et al.* 1987). Even though $c = 0.01$, we must keep c as a specifiable parameter in models for liquid-metal magnetohydrodynamic flows in ducts with metal walls (Talmage & Walker 1988).

Moon & Walker (1988) present the first analytical model for liquid flow through an elbow in the plane of a uniform magnetic field. They treat the flow in two straight ducts connected by a gradual elbow with a large radius of curvature. For an extremely large radius of curvature, the flow is locally fully developed at each cross-section, and there is no additional pressure drop associated with three-dimensional effects. For a moderately large radius of curvature, the flow deviates from fully developed with a decrease in velocity near the centre and an increase near the walls which are parallel to the magnetic field. There is also a significant three-dimensional pressure drop. Unfortunately, the analysis of Moon & Walker (1988) cannot be extrapolated to a radius of curvature which is comparable to the cross-sectional dimensions of the duct. If we attempt such an extrapolation, the analysis predicts unrealistically severe flow distributions and unrealistically large three-dimensional pressure drops. A quite different model is needed for an elbow with a small radius of curvature or for a sharp elbow. Here we treat the flow in a sharp 90° elbow, but the

analysis applies equally well for two straight ducts connected by a small-radius elbow. Only minor details in the finite-difference solution presented in §4 are different for the small-radius elbow.

In §2, the three-dimensional problem is reduced to a problem involving four coupled two-dimensional functions: the electrical potential functions in three walls and the pressure in the bulk of the liquid metal. There are three axially sequential sectors in the geometry and different solution techniques are appropriate for different sectors. A separation of variables solution for the first and third sectors is presented in §3. This solution is also a quite general solution for any three-dimensional flow in a constant-area, rectangular duct in a skewed, uniform magnetic field. Previous analyses for three-dimensional liquid-metal duct flows with strong magnetic fields have all assumed a symmetry about a plane which is perpendicular to the magnetic field, except the analysis of Moon & Walker (1988). The solution presented in §3 reveals that such symmetric flows represent a very singular case. With even a slight deviation from this perfect symmetry, the mathematical characteristics of the solution are quite different. The present solution is the first full solution for a three-dimensional magnetohydrodynamic flow which is not symmetric about a plane normal to the magnetic field. A finite-difference relaxation solution for the second sector and the coupling with the first and third sectors are presented in §4. The results for $c = 0.01$–1.0 are presented in §5. Our objective is to treat a basic problem in magnetohydrodynamics, so we consider values of c beyond those arising in fusion reactor cooling systems. The results show that the flow distribution is not particularly severe for any case considered and that the flow becomes fully developed in a short distance on both sides of the elbow. The additional pressure drop due to three-dimensional effects is also presented.

2. Problem formulation

We treat a liquid-metal flow in a metal duct with a strong, uniform, applied magnetic field, $B_0\hat{\boldsymbol{y}}$, where B_0 is the magnetic flux density, and $\hat{\boldsymbol{x}}$, $\hat{\boldsymbol{y}}$, $\hat{\boldsymbol{z}}$ are unit vectors for Cartesian coordinates. The electric currents in the liquid metal and in the metal duct walls create an additional, induced magnetic field, which can be neglected if the magnetic Reynolds number, $R_m = \mu_p \sigma U_0 L \ll 1$. Here μ_p and σ are the magnetic permeability and electrical conductivity of the liquid metal, while U_0 and L are the characteristic velocity and length. With this assumption, the dimensionless equations governing the steady flow of a liquid metal with constant properties are

$$N^{-1}(\boldsymbol{v}\cdot\boldsymbol{\nabla})\,\boldsymbol{v} = -\boldsymbol{\nabla}p + \boldsymbol{j}\times\hat{\boldsymbol{y}} + M^{-2}\nabla^2\boldsymbol{v}, \tag{1a}$$

$$\boldsymbol{j} = -\boldsymbol{\nabla}\phi + \boldsymbol{v}\times\hat{\boldsymbol{y}}, \quad \boldsymbol{\nabla}\cdot\boldsymbol{v} = 0, \quad \boldsymbol{\nabla}\cdot\boldsymbol{j} = 0. \tag{1b–d}$$

Here $\boldsymbol{v}$, p, $\boldsymbol{j}$ and ϕ are the fluid velocity, pressure, electric current density and electric potential function, which are normalized by U_0, $\sigma U_0 B_0^2 L$, $\sigma U_0 B_0$ and $U_0 B_0 L$, respectively. The interaction parameter and Hartmann number are

$$N = \sigma B_0^2 L/\rho U_0, \quad M = B_0 L(\sigma/\mu)^{\frac{1}{2}},$$

where ρ and μ are the density and viscosity of the liquid metal. For a sufficiently strong applied magnetic field, $N \gg 1$ and $M \gg 1$, so that the inertial and viscous terms in the momentum equation (1 a) can be neglected except in thin boundary and interior layers where velocity gradients become large.

The present geometry consists of two identical, semi-infinite, constant-area,

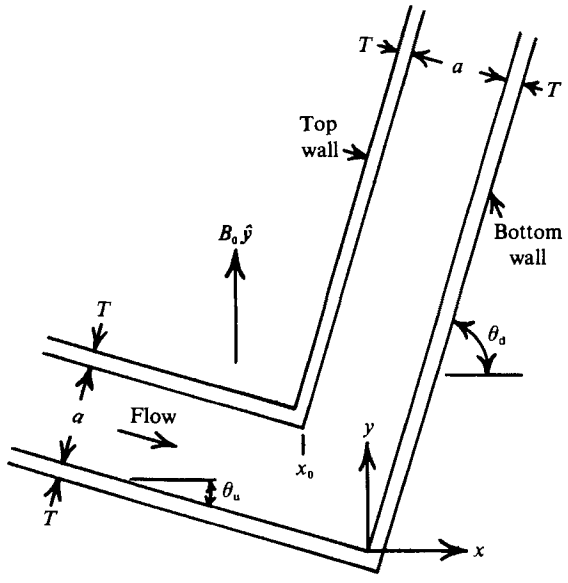

FIGURE 1. Vertical section of a sharp elbow in the plane of a uniform magnetic field. There are sides with dimensionless thickness T_s at $z = \pm 1$. Here $\theta_u = \theta_d - 90°$ for a 90° mitre corner.

rectangular ducts with one end bevelled at 45° and joined to form a 90° sharp mitre corner, as shown in figure 1. The top and bottom walls of both semi-infinite ducts are parallel to the z-axis, are separated by a dimensionless distance a and have a dimensionless thickness T. The angle between the x-axis and the downstream top or bottom is θ_d, where $45° \leqslant \theta_d < 90°$, while the angle between the x-axis and the upstream top or bottom is $\theta_u = \theta_d - 90°$, where $-45° \leqslant \theta_u < 0°$. The other pair of walls are the sides which are parallel to the magnetic field, which have a dimensionless thickness T_s and which have inside surfaces at $z = \pm 1$, because L is half the distance between the sides. The flow is symmetric about the plane midway between the sides, so that we need only treat the flow for $-1 \leqslant z \leqslant 0$, with appropriate symmetry conditions at $z = 0$.

Following Shercliff (1956), we assume that $T_s \ll 1$, so that the boundary conditions at the side are

$$v = 0, \quad j_z = c_s\left(\frac{\partial^2\phi_s}{\partial x^2} + \frac{\partial^2\phi_s}{\partial y^2}\right), \quad \text{at } z = -1, \tag{2a, b}$$

where $c_s = \sigma_w T_s/\sigma$ is the sidewall conductance ratio, σ_w is the electrical conductivity of the metal duct walls, and $\phi_s(x, y)$ is the electric potential function in the side, which is independent of z neglecting $O(T_s^2)$ terms. Similarly we assume that $T \ll 1$, so that the boundary conditions at the bottom walls are

$$\left.\begin{aligned} v &= 0 \qquad\qquad\qquad\qquad\qquad\qquad (3a)\\ \cos\theta j_y - \sin\theta j_x &= c\left(\cos^2\theta\frac{\partial^2\phi_b}{\partial x^2} + \frac{\partial^2\phi_b}{\partial z^2}\right) \qquad (3b)\end{aligned}\right\} \quad \text{at } y = f_b,$$

where $c = \sigma_w T/\sigma$ is the wall conductance ratio for the top or bottom, $y = f_b(x) = x\tan\theta$ is the location of the inside surface of the bottom, and $\phi_b(x, z)$ is the electric potential function in the bottom wall, which is uniform through the wall thickness

neglecting $O(T^2)$ terms, while $\theta = \theta_d$ for $x > 0$ and $\theta = \theta_u$ for $x < 0$. The boundary conditions at the top walls are

$$\left.\begin{aligned} v &= 0 \qquad (4a)\\ \sin\theta j_x - \cos\theta j_y &= c\left(\cos^2\theta\frac{\partial^2\phi_t}{\partial x^2}+\frac{\partial^2\phi_t}{\partial z^2}\right) \qquad (4b)\end{aligned}\right\} \quad \text{at } y = f_t,$$

where $y = f_t(x) = x\tan\theta + a\sec\theta$ is the location of the inside surface of the top wall and $\phi_t(x,z)$ is the electric potential function in the top wall, while $\theta = \theta_d$ for $x > x_0 = a(\cos\theta_d - \sin\theta_d) < 0$, and $\theta = \theta_u$ for $x < x_0$.

We choose the average velocity parallel to the centreline of either semi-infinite duct away from the junction as U_0, so that the dimensionless velocity must satisfy the volume flux condition

$$\int_{f_b}^{f_t}\int_{-1}^{0} u(x,y,z)\,dz\,dy = a, \qquad (5)$$

at each x = constant section, where $\boldsymbol{v} = u\hat{\boldsymbol{x}} + v\hat{\boldsymbol{y}} + w\hat{\boldsymbol{x}}$. The condition (5) scales the solution of the homogeneous boundary-value problem (1–4).

For $M \gg 1$ and $N \gg 1$, there are two interior or free shear layers which completely span the flow at the $x = x_0$ and $x = 0$ sections. Hunt & Leibovich (1967) show that the characteristic dimensionless thickness δ of such interior layers is $M^{-\frac{1}{2}}$ if $N \gg M^{\frac{3}{2}}$ or $N^{-\frac{1}{3}}$ is $N \ll M^{\frac{3}{2}}$. The two interior layers separate three axially successive sectors of the geometry. With the present coordinate system which is oriented with the applied magnetic field, sector 1 for $x < x_0$ and sector 3 for $x > 0$ represent constant-area, rectangular ducts in a skewed magnetic field, while sector 2 for $x_0 < x < 0$ represents an asymmetric expansion. In each sector, there is an inviscid, inertialess core region which is separated from the top and bottom walls by Hartmann layers and from the sidewall by a side layer. The Hartmann layers have an $O(M^{-1})$ dimensionless thickness and their local, exponential structure is well known. They match the core solution and satisfy the conditions (3a, 4a), provided the core variables satisfy the Hartmann condition

$$v = \tan\theta u, \quad \text{at } y = f_b, \quad y = f_t, \qquad (6a, b)$$

neglecting $O(M^{-1})$ terms. Again, θ switches from θ_u to θ_d at $x = 0$ for the bottom wall and at $x = x_0$ for the top wall. Walker, Ludford & Hunt (1972) show that the jumps in the electric potential function and in the normal component of the electric current density are $O(M^{-2})$ and $O(M^{-1})$ across a Hartmann layer, so that the conditions (3b, 4b) can be applied to the core variables neglecting $O(M^{-1})$ terms.

For the core regions in all three sectors, the solution of (1), neglecting the inertial and viscous terms, is

$$j_{xc} = \frac{\partial p_c}{\partial z}, \quad j_{yc} = -\frac{\partial\phi_c}{\partial y}, \quad j_{zc} = -\frac{\partial p_c}{\partial x}, \qquad (7a\text{–}c)$$

$$u_c = \frac{\partial\phi_c}{\partial z} - \frac{\partial p_c}{\partial x}, \quad w_c = -\frac{\partial\phi_c}{\partial x} - \frac{\partial p_c}{\partial z}, \qquad (7d, e)$$

$$v_c = (y - f_b)\left(\frac{\partial^2 p_c}{\partial x^2} + \frac{\partial^2 p_c}{\partial z^2}\right) + g_c, \qquad (7f)$$

$$\phi_c = \phi_b + (\phi_t - \phi_b)(y - f_b)/(f_t - f_b), \qquad (7g)$$

where $p_c(x,z)$ and $g_c(x,z)$ are integration functions and the subscript c denotes a core variable. When the conditions (3b, 4b, 6) are applied to the core variables (7), they

yield four equations governing ϕ_t, ϕ_b, p_c and g_c, which are only functions of x and z. The resultant equations are different for different sectors. For the core regions in sectors 1 and 3, we obtain

$$g_c = \tan\theta\left(\frac{\partial\phi_b}{\partial z} - \frac{\partial p_c}{\partial x}\right), \tag{8a}$$

$$a\left(\frac{\partial^2 p_c}{\partial x^2} + \frac{\partial^2 p_c}{\partial z^2}\right) = \sin\theta\left(\frac{\partial\phi_t}{\partial z} - \frac{\partial\phi_b}{\partial z}\right), \tag{8b}$$

$$c\left(\cos^2\theta\frac{\partial^2\phi_b}{\partial x^2} + \frac{\partial^2\phi_b}{\partial z^2}\right) = \cos\theta j_{yc} - \sin\theta\frac{\partial p_c}{\partial z}, \tag{8c}$$

$$c\left(\cos^2\theta\frac{\partial^2\phi_t}{\partial x^2} + \frac{\partial^2\phi_t}{\partial z^2}\right) = \sin\theta\frac{\partial p_c}{\partial z} - \cos\theta j_{yc}, \tag{8d}$$

$$j_{yc} = a^{-1}\cos\theta\,(\phi_b - \phi_t), \tag{8e}$$

where $\theta = \theta_d$ for sector 3 and $\theta = \theta_u$ for sector 1. For the core in sector 2, g_c is again given by (8a) with $\theta = \theta_u$, and

$$(x + a\sin\theta_d)\left(\frac{\partial^2 p_c}{\partial x^2} + \frac{\partial^2 p_c}{\partial z^2}\right) + \frac{\partial p_c}{\partial x} = \sin^2\theta_d\frac{\partial\phi_t}{\partial z} + \cos^2\theta_d\frac{\partial\phi_b}{\partial z}, \tag{9a}$$

$$c\left(\sin^2\theta_d\frac{\partial^2\phi_b}{\partial x^2} + \frac{\partial^2\phi_b}{\partial z^2}\right) = \cos\theta_d\frac{\partial p_c}{\partial z} + \sin\theta_d j_{yc}, \tag{9b}$$

$$c\left(\cos^2\theta_d\frac{\partial^2\phi_t}{\partial x^2} + \frac{\partial^2\phi_t}{\partial z^2}\right) = \sin\theta_d\frac{\partial p_c}{\partial z} - \cos\theta_d j_{yc}, \tag{9c}$$

$$j_{yc} = \cos\theta_d(\phi_b - \phi_t)/(a + x\,\mathrm{cosec}\,\theta_d), \tag{9d}$$

where θ_d is used throughout sector 2 to avoid the confusion of different θ for the top and bottom walls. The purpose of introducing both θ_d and θ_u is to reduce the boundary-value problems for sectors 1 and 3 to the same problem for an arbitrary θ. The symmetry conditions are

$$\phi_t = 0, \quad \phi_b = 0, \quad \partial p_c/\partial z = 0 \quad \text{at } z = 0. \tag{10a–c}$$

The velocities in the interior layers at $x = x_0$ and at $x = 0$ are at most $O(1)$, i.e. there are no large, $O(\delta^{-1})$ velocities inside these layers. Neglecting $O(\delta)$ terms, all variables are continuous across the interior layers except v and w, and the role of these layers is to match discontinuities in v and w between adjacent core regions. Therefore, ϕ_t, ϕ_b, p_c and $\partial p_c/\partial x$ are the same in cores 1 and 2 at $x = x_0$ and are the same in cores 2 and 3 at $x = 0$. The continuity of u_c and j_{zc} imply the continuity of $\partial p_c/\partial x$. In addition, the interior layers cannot accept any $O(1)$ electric current from the top or bottom walls, so that the currents along these walls must be continuous at $x = x_0$ and $x = 0$. This continuity of electric currents in the top and bottom gives the matching conditions

$$\frac{\partial\phi_{b1}}{\partial x} = \frac{\partial\phi_{b2}}{\partial x}, \quad \cos\theta_u\frac{\partial\phi_{t1}}{\partial x} = \cos\theta_d\frac{\partial\phi_{t2}}{\partial x} \quad \text{at } x = x_0, \tag{11a, b}$$

$$\cos\theta_u\frac{\partial\phi_{b2}}{\partial x} = \cos\theta_d\frac{\partial\phi_{b3}}{\partial x}, \quad \frac{\partial\phi_{t2}}{\partial x} = \frac{\partial\phi_{t3}}{\partial x} \quad \text{at } x = 0, \tag{11c, d}$$

where the numerical subscript denotes the sector.

Like the interior layers, the side layers in all three sectors have a dimensionless thickness δ which is $N^{-\frac{1}{3}}$ if $N \ll M^{\frac{3}{2}}$ or $M^{-\frac{1}{2}}$ if $N \gg M^{\frac{3}{2}}$. For either case, u_{SL} and v_{SL} are $O(\delta^{-1})$; ϕ_{SL}, w_{SL}, $j_{x\mathrm{SL}}$ and $j_{y\mathrm{SL}}$ are $O(1)$; while

$$p = p_{\mathrm{c}}(x, -1) + \delta p_{\mathrm{SL}}(x, y, \zeta),$$

$$j_z = -\frac{\partial p_{\mathrm{c}}}{\partial x}(x, -1) + \delta j_{z\mathrm{SL}}(x, y, \zeta),$$

where $\zeta = \delta^{-1}(z+1)$ is the stretched side-layer coordinate and the subscripts SL denote the leading term in the asymptotic expansion for a side-layer variable. If $\delta \ll c_{\mathrm{s}}$, i.e. if we assume that c_{s} is an $O(1)$ parameter, while $N \gg 1$ and $M \gg 1$, then the condition $(2b)$ becomes an equation governing the electric potential function $\phi_{\mathrm{s}}(x, y)$ in the sidewall,

$$c_{\mathrm{s}}\left(\frac{\partial^2 \phi_{\mathrm{s}}}{\partial x^2} + \frac{\partial^2 \phi_{\mathrm{s}}}{\partial y^2}\right) = -\frac{\partial p_{\mathrm{c}}}{\partial x}(x, -1). \tag{12}$$

With $\delta \ll c_{\mathrm{s}}$, we can solve for the core variables and wall potentials without obtaining a detailed solution for the side-layer variables, but several characteristics of the side layers are important. Since u_{SL} is $O(\delta^{-1})$, the volume flux inside the side layers is comparable to that in the cores. The $O(\delta^{-1})$ terms in the z-component of Ohm's law $(1b)$ give $u_{\mathrm{SL}} = \partial \phi_{\mathrm{SL}}/\partial \zeta$, so that the volume flux in a unit Δy of a side layer is

$$\int_0^\infty u_{\mathrm{SL}}(x, y, \zeta)\, \mathrm{d}\zeta = \phi_{\mathrm{c}}(x, y, -1) - \phi_{\mathrm{s}}(x, y). \tag{13}$$

Therefore, the solutions for ϕ_{t}, ϕ_{b} and ϕ_{s} determine the volume flux inside the side layer without the solution for u_{SL}. In other words, the difference in electric potential between the core and side determines the total flow inside the side layer, whether inertial or viscous effects dominate for $N \ll M^{\frac{3}{2}}$ or $N \gg M^{\frac{3}{2}}$, respectively. When the core solution $(7d)$ and the integral (13) are introduced into the volume flux condition (5), this condition becomes

$$\int_{f_{\mathrm{b}}}^{f_{\mathrm{t}}} \phi_{\mathrm{s}}(x, y)\, \mathrm{d}y + (f_{\mathrm{t}} - f_{\mathrm{b}}) \int_{-1}^{0} \frac{\partial p_{\mathrm{c}}}{\partial x}(x, z)\, \mathrm{d}z = -a. \tag{14}$$

The condition (14) guarantees that the solutions for ϕ_{s} and p_{c} are compatible with the side-layer boundary-value problem, so that the latter can be ignored if the condition (14) is satisfied. For $N \gg M^{\frac{3}{2}}$, the side-layer solution is given by an extension of the separation of variables solution of Hunt (1965), but no solution for a side layer with $N \ll M^{\frac{3}{2}}$ has been published to date.

Since $j_{y\mathrm{SL}}$ is $O(1)$, the total current between the side layer and the adjacent segment of the top or bottom is $O(\delta)$, while the variation of ϕ_{t} and ϕ_{b} over the thickness of the side layer is $O(\delta)$. Therefore, the electric potential must be continuous at the corners, $y = f_{\mathrm{b}}$, $z = -1$ and $y = f_{\mathrm{t}}$, $z = -1$. In addition, the electric current entering a corner from the side must equal the electric current entering the top or bottom from that corner, because the TT_{s} cross-sectional area of the corner is too small to carry significant axial current. For sectors 1 and 3, the continuity of potential and current requires that

$$\left.\begin{aligned} \phi_{\mathrm{s}} &= \phi_{\mathrm{b}}(x, -1) && (15a) \\ c_{\mathrm{s}}\left(\sin\theta \frac{\partial \phi_{\mathrm{s}}}{\partial x} - \cos\theta \frac{\partial \phi_{\mathrm{s}}}{\partial y}\right) &= c \frac{\partial \phi_{\mathrm{b}}}{\partial z}(x, -1) && (15b) \end{aligned}\right\} \quad \text{at } y = f_{\mathrm{b}} = x\tan\theta,$$

$$\left.\begin{aligned} \phi_s &= \phi_t(x,-1) \\ c_s\left(\cos\theta\frac{\partial\phi_s}{\partial y}-\sin\theta\frac{\partial\phi_s}{\partial x}\right) &= c\frac{\partial\phi_t}{\partial z}(x,-1) \end{aligned}\right\} \quad \text{at } y = f_t = x\tan\theta + a\sec\theta, \tag{15c,d}$$

where $\theta = \theta_d$ for sector 3 and $\theta = \theta_u$ for sector 1. For sector 2, the conditions (15*a*, *b*) apply with $\theta = \theta_u = \theta_d - 90°$, and the conditions (15*c*, *d*) apply with $\theta = \theta_d$.

The interior layers at $x = x_0$ and at $x = 0$ cannot accept any $O(1)$ current from the side, so that ϕ_s and $\partial\phi_s/\partial x$ are continuous at $x = x_0$ and $x = 0$. The two-dimensional variables p_c, ϕ_t, ϕ_b and ϕ_s are governed by equations (8), (9), (12) and by the conditions (10), (14), (15) in each of the three sectors. The solutions in different sectors are coupled by the continuity of ϕ_t, ϕ_b, p_c, ϕ_s, $\partial p_c/\partial x$ and $\partial\phi_s/\partial x$ at $x = x_0$ and at $x = 0$, as well as by the matching conditions (11). The separation of variables solution for sectors 1 and 3 is presented in §3, while the finite-difference solution for sector 2 and the Galerkin-conservation integral coupling at $x = x_0$ and $x = 0$ are presented in §4.

3. Three-dimensional flow in a constant-area duct with a skewed magnetic field

The solution for sectors 1 and 3 is also a general solution for any three-dimensional flow in a constant-area, rectangular duct with its centreline at an arbitrary angle $(90°-\theta)$ to the direction of a uniform magnetic field. The equations (8), (12) and symmetry conditions (10) are satisfied by the separation of variables solutions

$$p_c = C_0 - \frac{2cKx}{a} + \sum_{n=1}^{\infty} C_n \exp(-\lambda_n x)[A_n \cos(\lambda_n \cos\theta z) + B_n \cosh(\alpha_n z)], \tag{16a}$$

$$\phi_t + \phi_b = 2Kz + \sum_{n=1}^{\infty} C_n \exp(-\lambda_n x)\sin(\lambda_n \cos\theta z), \tag{16b}$$

$$\phi_t - \phi_b = \sum_{n=1}^{\infty} C_n \exp(-\lambda_n x)\left[a\lambda_n \tan\theta A_n \sin(\lambda_n \cos\theta z) + \frac{2B_n \sinh(\alpha_n z)}{c\alpha_n \sin\theta}\right], \tag{16c}$$

$$\begin{aligned} \phi_s = {} & -K[1 + c\cos^2\theta Y(a\sec\theta - Y)/a^2] + \sum_{n=1}^{\infty} C_n \exp(-\lambda_n x) \\ & \times \{[A_n \cos(\lambda_n \cos\theta) + B_n \cosh(\alpha_n)]/\lambda_n c_s + \exp(-\lambda_n \cos\theta \sin\theta Y) \\ & \times [D_n \cos(\lambda_n \cos^2\theta Y) + E_n \sin(\lambda_n \cos^2\theta Y)]\}, \end{aligned} \tag{16d}$$

where $K = \cos\theta/(1 + 2c/a + ac/6c_s)$, $\alpha_n = (2/ac - \lambda_n^2)^{\frac{1}{2}}$, and $Y = y - x\tan\theta$. The terms before the summations in the solutions (16) represent fully developed flow in this constant-area duct. For each n, the constants in p_c, $(\phi_t - \phi_b)$ and ϕ_s are expressed as multiples of C_n, the constant in $(\phi_t + \phi_b)$. Here, λ_n is a set of discrete eigenvalues, the terms after $\exp(-\lambda_n x)$ in the expressions (16) are the corresponding eigenfunctions with the constants A_n, B_n, D_n and E_n, and the constants C_n are the coefficients of the eigenfunctions for each λ_n.

When we introduce the solutions (16) into the conditions (14), (15), we obtain five coupled equations which are linear in A_n, B_n, D_n and E_n. These five equations are

reduced to explicit expressions for A_n, B_n, D_n and E_n, and to a transcendental characteristic equation for the eigenvalues λ_n,

$$\begin{aligned}
&[2a\lambda_n \sin\theta(ac\alpha_n^2 \tan\theta R_1 - R_2) + 2R_8/c + \alpha_n^2 \sec\theta R_7/\lambda_n] \\
&\quad \times \cos(\lambda_n \cos\theta) \sinh(\alpha_n)/\alpha_n + 2\sec\theta R_4(\cos\theta R_5/\lambda_n - aR_1) \\
&\quad \times \cos(\lambda_n \cos\theta) \cosh(\alpha_n)/c_s\lambda_n + c_s[a\lambda_n \sec\theta R_4 R_6/c \\
&\quad + a\alpha_n^4 R_3 R_5/\lambda_n - 2ac_s\lambda_n \sec\theta R_1 R_4 \tan(\lambda_n \cos\theta)/c^2 \\
&\quad + 4aR_1/c^2] \sin(\lambda_n \cos\theta) \sinh(\alpha_n)/\alpha_n + [R_7 - \lambda_n R_3 R_8 \\
&\quad + 2a\sec\theta(\sin\theta R_2 + 2\cos\theta R_1) + a\sec\theta R_4 R_5/c\lambda_n \\
&\quad - 2ac_s(\cos^2\theta R_5 + \lambda_n R_1 R_3)\tan(\lambda_n \cos\theta)/c] \\
&\quad \times \sin(\lambda_n \cos\theta) \cosh(\alpha_n) = D(a, c, c_s, \theta, \lambda_n) = 0, \qquad (17)
\end{aligned}$$

where

$$R_1 = \exp(-a\lambda_n \sin\theta) \sin(a\lambda_n \cos\theta), \qquad (18a)$$

$$R_2 = 1 - \exp(-2a\lambda_n \sin\theta), \quad R_3 = a\tan\theta \sin\theta, \qquad (18b, c)$$

$$R_4 = 2 - ac\lambda_n^2 \sin^2\theta, \qquad (18d)$$

$$R_5 = 1 - 2\exp(-a\lambda_n \sin\theta)\cos(a\lambda_n \cos\theta) + \exp(-2a\lambda_n \sin\theta), \qquad (18e)$$

$$R_6 = R_5 + 4\exp(-a\lambda_n \sin\theta)\cos(a\lambda_n \cos\theta), \qquad (18f)$$

$$R_7 = 2a\sin\theta(\cos\theta R_2 - 2\sin\theta R_1), \qquad (18g)$$

$$R_8 = 2(\sin\theta R_2 + 2\cos\theta R_1)/\lambda_n - aR_6. \qquad (18h)$$

The rather complicated explicit expressions for A_n, B_n, D_n and E_n from the conditions (14), (15) are not presented here, but are presented by Moon (1989). Once we find an eigenvalue λ_n which satisfies the characteristic equation (17), these expressions give the corresponding values of A_n, B_n, D_n and E_n, so that everything is known for this eigenvalue except the coefficient C_n.

For each set of values for a, c, c_s and θ, there is an infinite set of discrete eigenvalues λ_n which satisfy the equation (17). A duct in a perfectly transverse magnetic field with $\theta = 0$ is a very singular case. For $\theta = 0$, all eigenvalues are real and are symmetric about the double root $\lambda_0 = 0$, corresponding to fully developed flow. The eigenfunctions separate into: (i) even modes with $\phi_t = \phi_b$ and ϕ_s as an even function of $(y - \frac{1}{2}a)$, and (ii) odd modes with $\phi_t = -\phi_b$, $p_c = 0$ and ϕ_s as an odd function of $(y - \frac{1}{2}a)$. To illustrate the evolution of the eigenvalues as θ begins to deviate from zero, we consider a typical case with $a = c = c_s = 1$. For this case with $\theta = 0$, there are no double roots except $\lambda_0 = 0$, but the eigenvalues include certain pairs which are very close to $2\pi m$, for $m = 1, 2, 3, \ldots$. Each of these pairs consist of an even mode and an odd mode. As we begin to increase or decrease θ from zero, these pairs begin to come together on the real axis and then branch into pairs of complex conjugates in the complex λ plane. The transition to complex conjugate eigenvalues begins with the pairs near large multiples of 2π and moves successively to the pair near 2π as the magnitude of θ increases. However, all of these pairs have become complex before $|\theta| = 1°$. Therefore, a duct with a perfectly transverse magnetic field and $\theta = 0$ is a very special case with all real eigenvalues. For a very slight misalignment with $\theta = \pm 1°$, a significant fraction of the eigenvalues are complex conjugates. Previous studies of three-dimensional liquid-metal flows in strong magnetic fields have all assumed that the flow is symmetric about a plane which is perpendicular to the applied magnetic

field. The present results show that such symmetric flows represent special cases and that realistic flows with even slight misalignments have quite different mathematical characteristics.

As $|\theta|$ increases beyond 1°, other pairs of real eigenvalues come together on the real axis and branch into complex conjugates. The search over the complex $\lambda = \lambda_r + i\lambda_i$ plane for a given θ is facilitated by certain eigenvalue patterns. Since complex eigenvalues always occur as complex conjugates, we need only search the upper half plane, $\lambda_i \geqslant 0$. All eigenvalues lie either on the real axis or along a single curve in each quadrant of the complex plane. The curve in the first or fourth quadrant approaches a straight line away from the origin. The complex eigenvalues approach an equal spacing along each curve.

For a given set of values for a, c, c_s and θ, we first find the real eigenvalues. We compute the real values of D given by (17) at successive real values of λ. When D switches signs, we have passed an eigenvalue, and a modified Newton–Raphson method quickly converges to that eigenvalue. For $\lambda_i > 0, D = D_r + iD_i$, so we begin by plotting rough curves for $D_r = 0$ and $D_i = 0$ in the first or fourth quadrant. The intersection of a $D_r = 0$ curve and a $D_i = 0$ curve indicates the neighbourhood of a complex eigenvalue. Since the complex D given by (17) is a regular function of the complex variable λ, a simple complex Newton–Raphson scheme determines the complex eigenvalue to 15 significant figures in less than 8 iterations once the approximate neighbourhood is known. Once the preliminary search with rough sketches of the $D_r = 0$ and $D_i = 0$ curves has identified the first four eigenvalues in one of the quadrants, then the single curve for the complex eigenvalues and their spacing along this curve are easily identified. Therefore we can estimate the neighbourhoods for all successive complex eigenvalues in that quadrant without plotting curves. Some eigenvalues for $a = c = c_s = 1$, $\theta = 84.29°$ ($\tan\theta = 10$) and $\lambda_r > 0$ are: 3.576, $4.918 \pm 4.623i$, 6.489, $7.006 \pm 11.01i$, $8.474 \pm 17.38i$, 9.579, $9.681 \pm 23.71i$, $10.75 \pm 30.00i$, $11.74 \pm 36.28i$, $12.67 \pm 42.55i$, 12.71, $13.56 \pm 48.81i$, $14.42 \pm 55.07i$, $15.26 \pm 61.33i$, 15.71, 15.93, $16.08 \pm 67.58i$. For this case, successive complex eigenvalues approach spacing along a straight line with $\Delta\lambda_r = 0.82$ and $\Delta\lambda_i = 6.25$. We number the eigenvalues by increasing magnitude of λ_r, corresponding to increasingly rapid spatial decay in x for the solutions (16). For sector 3, we keep only the eigenvalues with $\lambda_r > 0$ for $\theta = \theta_d$, and for sector 1, we keep only the eigenvalues with $\lambda_r < 0$ for $\theta = \theta_u$. Once we have determined the eigenvalues which satisfy the characteristic equation (17) and the corresponding values of the coefficients A_n, B_n, D_n and E_n, everything in the solutions (16) is known for sector 1 or sector 3 except the coefficients C_n which are determined by the coupling at $x = x_0$ or at $x = 0$, respectively.

4. Solution for sector 2 and coupling with sectors 1 and 3

A separation of variables solution is not possible for sector 2 because several coefficients in the equations (9) are functions of x and because the domain for (12) is a trapezoid. We use a finite-difference relaxation method to solve the equations (9), (12) and the conditions (10), (14), (15) with the values of p_c, ϕ_t, ϕ_b and ϕ_s at $x = x_0$ and at $x = 0$ treated as known values. For the side, the first row of grid points lies along the intersection with the bottom, and subsequent rows are parallel to the bottom. For integer values of $\tan\theta_d$, certain uniform spacings between rows lead to grid points along the intersection with the top wall. Each successive row which meets the top wall has one less grid point. We use the same x positions for the core and side,

and we stagger the grid in z for the core. Grid points for ϕ_t and ϕ_b are at $z = -1+j$ (Δz), while points for p_c are at $-1+(j+0.5)\,\Delta z$, for $j = 0, 1, 2, \ldots$. The staggered grid is introduced because of the mix of even and odd derivatives with respect to z in equations (9). We integrate equations (9) and (12) over appropriate cells for each grid point. The cells are rectangles for the core and parallelograms for the side. The line integrals over parts of the cell boundary and area integrals over the cell are evaluated with truncated Taylor series with coefficients expressed in terms of neighbouring grid values. For the potential values along the intersection between the top or bottom and the side, we combine the integral of $(9b, c)$ over half cells in the top or bottom with the integral of (12) over partial cells in the side. Near the top or bottom, these partial side cells are triangles or parallelograms, respectively. The combination of partial cell integrals in the top or bottom and side, leads to line integrals along the intersections of exactly the boundary conditions $(15b, d)$.

In the relaxation scheme, we compute values at $x = x_0 + kh$, for $k = 1, 2, 3, \ldots$, to $x = -h$, where h is the axial grid spacing. At each x, we solve for the core values from $z = -1$ to $z = 0$ and then solve for the side potentials. For the core, we solve simultaneously for three values: ϕ_t and ϕ_b at a point and p_c at the point $0.5\Delta z$ away. This simultaneous solution for three core values is used because solutions are desired for values of c as small as 0.01. If one value of p_c is the only unknown in the differenced form of $(9a)$, one value of ϕ_b is the only unknown in $(9b)$ and one value of ϕ_t is the only unknown in $(9c)$, then the truncation error is h^2/c. If the three values of p_c, ϕ_b and ϕ_t are unknown in each of the equations $(9a, b, c)$, and if the three values are determined simultaneously in terms of the values at the surrounding grid points, then the truncation error is h^2 for any value of c (Hua *et al.* 1988). This simultaneous relaxation scheme works quite well for $c = 0.001$ and $h = 0.1$.

For the coupling at $x = x_0$, we truncate the eigenfunction series (16) after the $n = (N1-1)$ terms, so that there are $N1$ unknowns for sector 1, namely C_n for $n = 0$ to $(N1-1)$. The $N2$ values of p_c, ϕ_b, ϕ_t and ϕ_s in sector 2 at the grid points at $x = x_0$ are also unknown, and we solve simultaneously for the $NT = (N1+N2)$ unknowns associated with the coupling at $x = x_0$. We use two types of linear, simultaneous equations to determine the NT unknowns. First, we use a Galerkin method to minimize the difference between the values of p_c, ϕ_b, ϕ_t and ϕ_s at $x = x_0$ from the separate sector 1 and sector 2 solutions. We define a residual

$$E = \int_{-1}^{0} [(p_{c1}-p_{c2})^2 + (\phi_{b1}-\phi_{b2})^2 + (\phi_{t1}-\phi_{t2})^2]\,dz + \int_{f_b}^{f_t} (\phi_{s1}-\phi_{s2})^2\,dy, \qquad (19)$$

where the subscript 1 denotes the sector 1 eigenfunction series (16) evaluated at $x = x_0$ and the subscript 2 denotes the sector 2 values at the grid points at $x = x_0$. We minimize the residual with respect to the series coefficients with

$$\partial E/\partial C_n = 0 \quad \text{for } n = 0 \text{ to } (N1-1). \qquad (20)$$

The equations (20) involve three types of terms. The first type of term involves one of the coefficients C_n times the sum of four integrals of products of the eigenfunctions in the series (16). Three integrals involve the eigenfunctions for p_c, ϕ_b and ϕ_t, integrated from $z = -1$ to $z = 0$, and the fourth integral involves the eigenfunctions for ϕ_s integrated from $y = f_b$ to $y = f_t$. These integrals are all evaluated analytically. The second type of term involves the sum of four integrals of an eigenfunction and a sector 2 solution at $x = x_0$. Since the sector 2 solution is only represented by the values at the grid points, we assume that each sector 2 value is constant over an interval centred at the grid point and we analytically integrate the eigenfunction

over the interval. These terms give known coefficients times the unknown values of p_{c2}, ϕ_{b2}, ϕ_{t2} and ϕ_{s2} at the grid points at $x = x_0$. The third type of term involves integrals of the eigenfunctions times the fully developed solution in the series (16), and these integrals are also evaluated analytically. The Galerkin matching of the values of p_c, ϕ_b, ϕ_t and ϕ_s at $x = x_0$ gives $N1$ linear, simultaneous, inhomogeneous equations with NT unknown values of the coefficients C_n and of the sector 2 grid values at $x = x_0$.

Equation (9*a*) ensures the conservation of mass for the core solution (7). When we integrate this equation over the cell centred at $x = x_0 + kh$ and $z = -1 + (j+0.5)(\Delta z)$, we are ensuring the conversation of mass for a rectangular prism which extends from $y = f_b$ to $y = f_t$ and which has a cross-sectional area of $h(\Delta z)$. The sector 2 relaxation scheme ensures conservation of mass for all such prisms between $x = x_0 + 0.5h$ and $x = -0.5h$. Similarly equations (9*b*), (9*c*) and (12) ensure conservation of electric current in the bottom, top and side, respectively, so that their differenced forms ensure the same conservation for appropriate segments of each wall between $x = x_0 + 0.5h$ and $x = -0.5h$. We must also ensure that mass and electric current are conserved in the interval $x_0 \leqslant x \leqslant x_0 + 0.5h$. We integrate (9) and (12) over half cells adjacent to the junction at $x = x_0$. The line integrals along the cell boundaries are evaluated from Taylor series as before, except the integral along the boundary at $x = x_0$. This integral involves the values of $\partial p_{c2}/\partial x$, $\partial \phi_{b2}/\partial x$, $\partial \phi_{t2}/\partial x$ and $\partial \phi_{s2}/\partial x$ in sector 2, evaluated at $x = x_0$. Using the continuity of $\partial p_c/\partial x$ and $\partial \phi_s/\partial x$ and the matching conditions (11*a*, *b*), the integrand is replaced by the values of $\partial p_{c1}/\partial x$, $\partial \phi_{b1}/\partial x$, $\partial \phi_{t1}/\partial x$ and $\partial \phi_{s1}/\partial x$ in sector 1 evaluated at $x = x_0$. Substituting the truncated eigenfunction series (16) into the line integrals along $x = x_0$, the values of the integrals are analytically determined in terms of the unknown coefficients C_n. The partial cells at the corners $x = x_0$, $y = f_b$ or f_t and $z = -1$ involve combinations of partial cells in the top or bottom and in the side which incorporate the continuity of electric current (3*b*), (4*b*) at the intersection of the side and top or bottom for $x_0 \leqslant x \leqslant x_0 + 0.5h$. Therefore, the integrals of (9) and (12) over partial cells adjacent to $x = x_0$ lead to $N2$ simultaneous, linear equations in which the coefficients C_n and the sector 2 values at the grid points at $x = x_0$ are unknowns and in which the values of p_c, ϕ_b, ϕ_t and ϕ_s at the grid points at $x = x_0 + h$ are treated as knowns.

The $N1$ equations from the Galerkin minimization of the residual (19) match the values of p_c, ϕ_b, ϕ_t and ϕ_s at the junction, while the $N2$ equations from the conservation integrals for partial cells match the axial derivatives at the junction. The $(NT \times NT)$ matrix of coefficients is inverted to give the values of C_n for sector 1 and the sector 2 values at the grid points at $x = x_0$ in terms of the fully developed flow at $x = -\infty$ and the sector 2 values at the grid points at $x = x_0 + h$. Therefore, the combination of the Galerkin method and the conservation integrals represents a global element which extends from $x = -\infty$ to $x = x_0 + 0.5h$ and which has NT degrees of freedom. The matching between the sector 2 and sector 3 solutions at $x = 0$ is exactly the same, except that there are more unknown values of the side potential at the grid points at $x = 0$ for $\theta_d > 45°$.

To begin the solution, we relax the sector 2 solution with fully developed flow values at $x = x_0$ and at $x = 0$, computed from the solutions (16) with $C_n = 0$, for $n \geqslant 1$, and with C_0 compute from an average of the sector 1 and sector 3 fully developed pressure gradients for the length $|x_0|$ of sector 2. After this initialization of the sector 2 values: (i) we update the sector 1 values of C_n and the sector 2 grid values at $x = x_0$, (ii) we sweep forward from $x = x_0 + h$ to $x = -h$ with the sector 2 relaxation scheme ten times, (iii) we update the sector 3 values of C_n and the sector 2 grid values

at $x = 0$, (iv) we sweep backward from $x = -h$ to $x_0 + h$ with the sector 2 relaxation scheme ten times, and (v) we repeat steps (i)–(iv) until the values of C_n for sectors 1 and 3 and the sector 2 grid values for $x_0 \leqslant x \leqslant 0$ have all converged. Since a constant pressure C_0 is included in both the sector 1 and sector 3 solutions (16), the arbitrary reference pressure is fixed by setting the pressure at one grid point in the interior of sector 2 equal to zero.

5. Results

There are two different fully developed flows far upstream and downstream of the elbow. The uniform core velocity parallel to the duct's centreline is the same in both fully developed flows,

$$v_{\parallel} = (1 + 2c/a)/(1 + 2c/a + ac/6c_s).$$

This core velocity and the transverse component of the magnetic field, $B_{\perp} = \cos\theta$, produce an induced electric field in the z-direction, $v_{\parallel}\cos\theta$, which represents the 'battery' for the electrical circuit. This battery drives electric currents through the liquid metal, sides and top or bottom, which are electrical resistances in series. The electric circuit is confined to cross-sections of the duct with positive and negative j_z in the core and top or bottom, respectively. The flow is symmetric about the plane midway between the top and bottom, so that the electric potentials of the top and bottom are the same and $j_x = j_y = 0$ in the core. The electric potentials and current densities are proportional to $\cos\theta_u$ and $\cos\theta_d$ for the upstream and downstream fully developed flows, respectively, where $\cos\theta_u = 10\cos\theta_d$ for the present duct.

Sector 2 and the disturbed portions of sectors 1 and 3 represent an electrical conductor placed between the two fully developed flows. In this three-dimensional flow, the strong upstream battery, $v_{\parallel}\cos\theta_u$, sees two electrical circuits in parallel: one through the sides and top or bottom in each cross-section and one with axial currents in the liquid metal and ducts walls in the $\pm x$-direction for $z \gtrless 0$. Downstream, the axial currents from the strong upstream battery overwhelm the weak downstream battery, $v_{\parallel}\cos\theta_d$, so that j_z in the core becomes negative for parts of sectors 2 and 3. This negative j_z completes the circuit for the axial currents from the upstream battery. Therefore, the three-dimensional current circulation is roughly given by the superposition of a current circulation in each cross-section and a three-dimensional current circulation in the disturbed region with $j_x \gtrless 0$ for $z \gtrless 0$ and with $j_z > 0$ upstream and $j_z < 0$ downstream. Upstream, the three-dimensional j_z augments the cross-sectional j_z, while downstream the former overwhelms the latter, giving a net negative j_z.

Equations (7 a, c) indicate that the core pressure $p_c(x, z)$ serves as a streamfunction for j_{xc} and j_{zc}, the components of the electric current density in the planes perpendicular to the magnetic field. For $a = 1.0$ and $c = c_s = 0.1$, plots of p_c versus x for $z = 0$, -0.85 and -1.0 are presented in figure 2. The upstream and downstream fully developed pressures, which are linear in x and independent of z, are achieved for $x < -3.0$ and $x > 0.3$, respectively. In sector 1 for $x < x_0 = -0.896$, the axial currents in the $\pm x$-direction for $z \gtrless 0$ produce an EM body force toward the sides. Since this body force is balanced by $\partial p_c/\partial z$, the centreline pressure is lower than p_c at $z = \pm 1$. The vertical distance between the top and bottom curves in figure 2 is proportional to the total core current in the $-x$-direction for $-1 \leqslant z \leqslant 0$, divided by the vertical distance between the top and bottom, $(f_t - f_b)$. Since the cross-sectional and three-dimensional transverse currents are additive upstream, the magnitudes of $-\partial p_c/\partial x$ are larger than that for the upstream fully developed flow in the disturbed

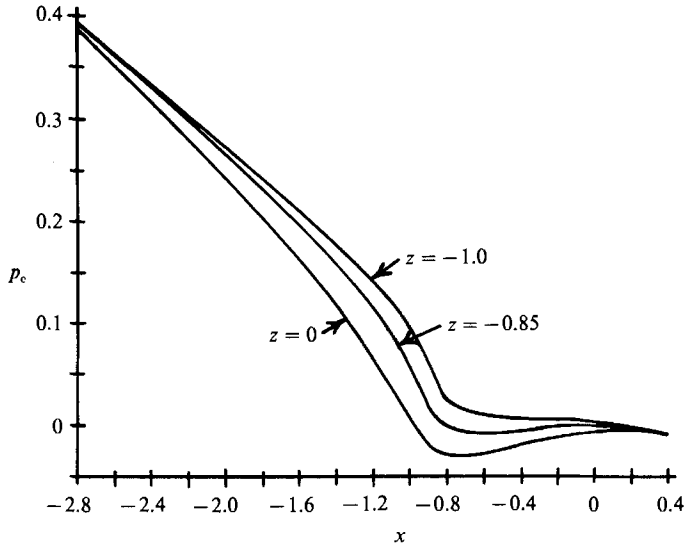

FIGURE 2. Core pressure p_c for $a = 1$ and $c = c_s = 0.1$. Plots of p_c versus x for $z = 0$, -0.85 and -1.0.

part of sector 1. In sector 2, the effective 'battery' strength decreases rapidly as the area in each x = constant plane increases, with corresponding decrease in u because of mass conservation. For $x > -0.8$, the three-dimensional j_z overwhelms the cross-sectional j_z, so that the net j_z is negative. This negative j_z completes the three-dimensional electric current circulation and produces a positive pressure gradient, $\partial p_c/\partial x > 0$, throughout the core, except very near $z = \pm 1$. At the junction of sectors 2 and 3 at $x = 0$, very little axial current remains and it completes its circuit in a short length of sector 3. The pressure at $z = -0.85$ is presented in figure 2 because p_c as a function of z is very flat near $z = 0$ and rises rapidly near $z = \pm 1$. For flow in the opposite direction through this elbow, the centreline pressure would be higher than p_c at $z = \pm 1$ in the disturbed region and the pressures are obtained by reflecting the curves in figure 2 about the $p = 0$ line.

To this point, the discussion of the pressures and electric currents applies qualitatively to many three-dimensional MHD duct flows between two different fully developed flows (see e.g. Hua *et al.* 1988). One special feature of the present geometry is its asymmetry about the $y = 0$ plane. Because of this asymmetry, a non-zero j_{xc} implies a non-zero j_{yc} and electric currents into or out of the top or bottom. The electric current density out of the top or bottom is equal to c times the Laplacian of the top or bottom potential on the wall surface, while j_{yc} is equal to the difference between the top and bottom potentials, divided by the local vertical distance between the top and bottom. In sector 2, the three-dimensional current circulation involves $j_{xc} < 0$ for $z < 0$. If sector 2 were a symmetric expansion, then ϕ_t would equal ϕ_b and j_{yc} would be zero. In this case, some of the axial current would enter the top and bottom at each cross-section, would flow to $z = -1$ in the top and bottom, would flow down or up the side and would then return to the core as j_{zc} at $z = -1$. Thus axial current in a symmetric, variable-area section is vertically redistributed through the duct walls. No vertical redistribution is possible in the core itself because $j_{yc} = 0$ (Walker 1981). The present sector 2 is a strongly asymmetric expansion: the top has a very steep slope of 10, while the bottom has a very small

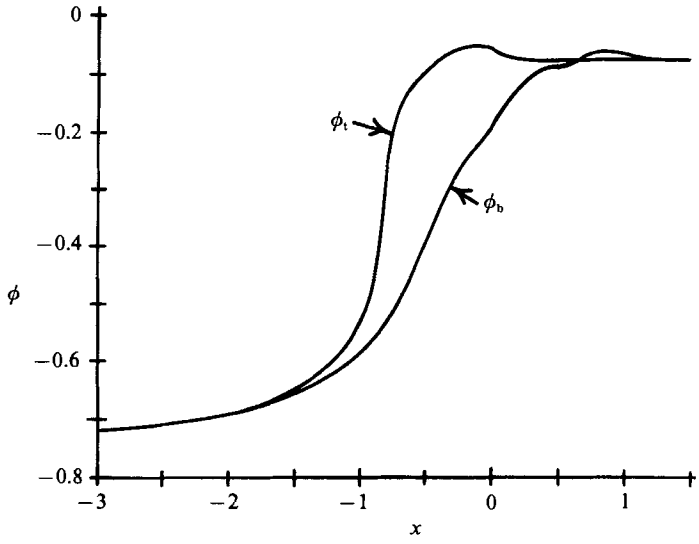

FIGURE 3. Top and bottom electric potential functions at $z = -1$ for $a = 1$ and $c = c_s = 0.1$.

slope of -0.1. The axial current $j_{xc} < 0$ for $z < 0$ implies a large negative j_{yc}, giving core current lines nearly parallel to the plane midway between the top and bottom at $\theta = \frac{1}{2}(\theta_u + \theta_d)$. Since j_{yc} is independent of y, some current enters the top and bottom at each cross-section and is vertically redistributed through the duct walls. The large negative j_{yc} implies that $\phi_b < \phi_t$ from (9*d*). The potential difference between the top and bottom and j_{yc} are illustrated by the plots of ϕ_t and ϕ_b at $z = -1$ for $a = 1$ and $c = c_s = 0.1$ in figure 3. Only values at $z = -1$ are presented because $\phi_t = \phi_b = 0$ at $z = 0$, both are linear in z for fully developed flow and both are generally curved with small slope near $z = 0$ and large slope near $z = -1$ for the disturbed regions. For fully developed flow $\phi_t = \phi_b$, and this is achieved for $x < -2.5$ and $x > 1.0$. The value of j_{yc} at $z = -1$ is given by the vertical distance between the two curves in figure 3, divided by $(f_t - f_b)$, which is much larger at $x = 0$ than at $x = x_0$. Throughout sector 2, $\phi_b < \phi_t$, so that $j_{yc} < 0$. Currents in sector 2 are sketched in figure 4. In sectors 1 and 3, the potential difference decays with distance from the junctions as the circuit is completed for the three-dimensional electric current circulation. In sector 3, there is a damped oscillation of ϕ_b, which reflects the fact that many eigenvalues for $\theta = 84.29°$ have imaginary parts which are larger than their real parts. For a short distance in sector 3, $\phi_b > \phi_t$, but this does not represent any significant current with $j_{yc} > 0$, since the vertical distance between the top and bottom is so large here.

Equations (7*d*, *f*, *g*) indicate that u_c and v_c are linear functions of y, while the boundary conditions (6) relate v_c and u_c at the top and bottom. Therefore, the values of u_c at $y = f_b$ and at $y = f_t$ determine the values of u_c and v_c everywhere, while the continuity equation (1*c*) then determines w_c. The plots of u_c at $y = f_b$, f_t and at $z = -0.05$, -0.95, for $a = 1$ and $c = c_s = 0.1$ are presented in figure 5. The values of u_c are given in figure 5, rather than the values of the velocity parallel to the walls, $v_\parallel$, because u_c is the only velocity which is continuous at $x = x_0$ and at $x = 0$, and because $v_\parallel$ represents two different directional velocities at the top and bottom of sector 2. However, v_c or $v_\parallel$ are easily obtained by multiplying u_c with the tangent or secant of the appropriate angle. At the top, u_c at $z = -0.95$ is larger than u_c at

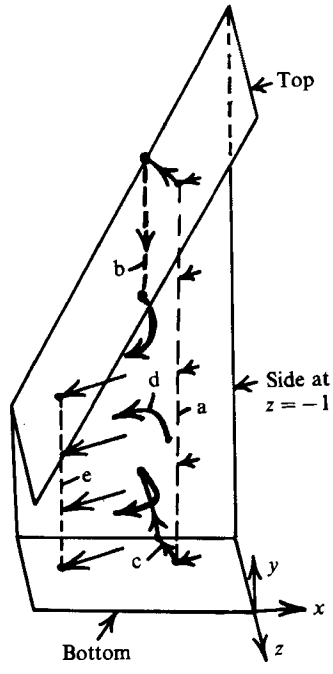

FIGURE 4. Sketch of electric currents in sector 2 for $z < 0$. Arrows along line a represent $j_{xc}\hat{x}+j_{yc}\hat{y}$ at a point (x, z) near $x = 0$. These currents are independent of y, so some current enters the top and bottom walls. The current entering the top or bottom flows to the junction with the side at $z = -1$, flows down or up the side, flows back into the liquid metal as $j_{xc}(x, -1)$ and finally turns to flow in the minus x-direction. These current paths are represented by the lines b and c. In addition there is current entering from the other half of the duct as $-j_{xc}(x, 0)$, which also turns to flow in the minus x-direction (line d). The arrows along the line e represent $j_{xc}\hat{x}+j_{yc}\hat{y}$ at an (x, z) near $x = x_0$. These arrows are larger than those at a because of the vertical current redistribution (lines b and c) and because of the current addition (line d).

$z = -0.05$ throughout the disturbed region. As the flow approaches $x = x_0$ in sector 1, it migrates towards $z = \pm 1$. As the flow moves through sector 2, it maintains a higher velocity near $z = \pm 1$ than at $z = 0$, but all values of u_c decrease as the vertical distance $(f_t - f_b)$ increases. Near $z = 0$, u_c drops to roughly a quarter of the value in the downstream fully developed flow and then the difference between the velocities at $z = \pm 1$ and at $z = 0$ decreases as the three-dimensional current completes its circuit. In sector 3, the transverse difference in u_c decays rapidly to zero. At the bottom, u_c in sector 1 is very similar to that at the top. In sector 2, u_c does not decrease as fast at the bottom as it does at the top, indicating that the flow is concentrated near the bottom in sector 2. This flow concentration near the bottom is associated with the large negative j_{yc} in sector 2 for $z < 0$. With $\phi_t = \phi_b = 0$ at $z = 0$ and with $\phi_b < \phi_t < 0$ at $z = -1$, $\partial\phi_b/\partial z$ is larger than $\partial\phi_t/\partial z$. Since $\partial p_c/\partial x$ is the same at the top and bottom, (7*d*) indicates that u_c must be larger near the bottom than at the top. Therefore, this flow concentration near the bottom in sector 2 results from the potential difference associated with the three-dimensional electric current circulation. As the flow approaches $x = 0$ in sector 2, the bottom u_c at $z = -0.95$ drops below that at $z = -0.05$ and both exhibit a damped oscillatory decay to the fully developed value in sector 3. Although u_c at the top at $z = -0.05$ becomes quite small in sector 2, this is not the smallest velocity along the top or bottom. The velocity along the top wall for $x > x_0$ is $u_c \sec\theta_d$, so that the velocity along the top

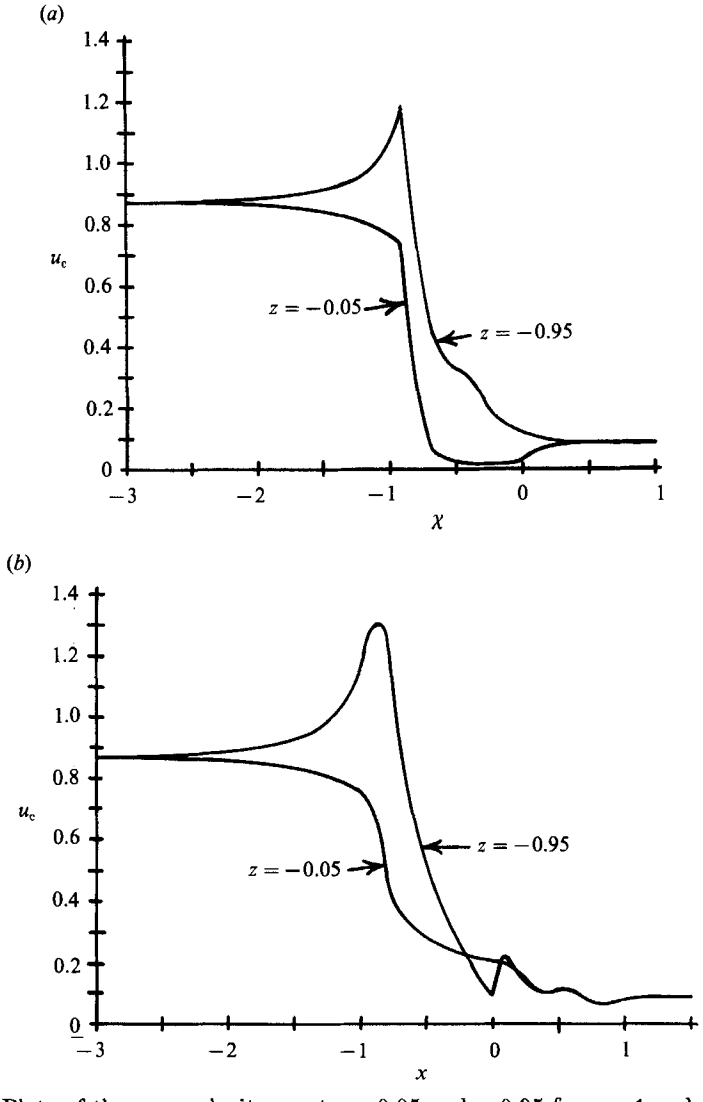

FIGURE 5. Plots of the core velocity u_c at $z = 0.05$ and -0.95 for $a = 1$ and $c = c_s = 0.1$ (*a*) at the top wall at $y = f_t$; (*b*) at the bottom wall at $y = f_b$.

in sector 2 is nowhere less than $0.2U_0$. The minimum velocity along any wall occurs in sector 2 near $x = 0$ and $z = -1$, where this velocity drops to roughly $0.1U_0$.

The results presented in figures 2, 3, 5 are for $c = c_s = 0.1$. If c and c_s are larger than 0.1, then the thicker walls allow more current to flow and the transition between the two fully developed flows involves less severe deviations from locally fully developed flow. If c and c_s are smaller than 0.1, then the transition involves more severe deviations from locally fully developed flows. Plots of u_c versus z at $x = -1$ and at $y = f_b$ are presented in figure 6 for $a = 1$ and for various equal values of c and c_s. Since this is the value of u_c at the bottom just inside sector 1, this is the velocity profile with the largest difference between the values of u_c at $z = 0$ and at $z = -1$. Even for $c = c_s = 0.01$, the velocity along the walls is nowhere zero or negative.

The additional pressure drop due to the three-dimensional effects associated with

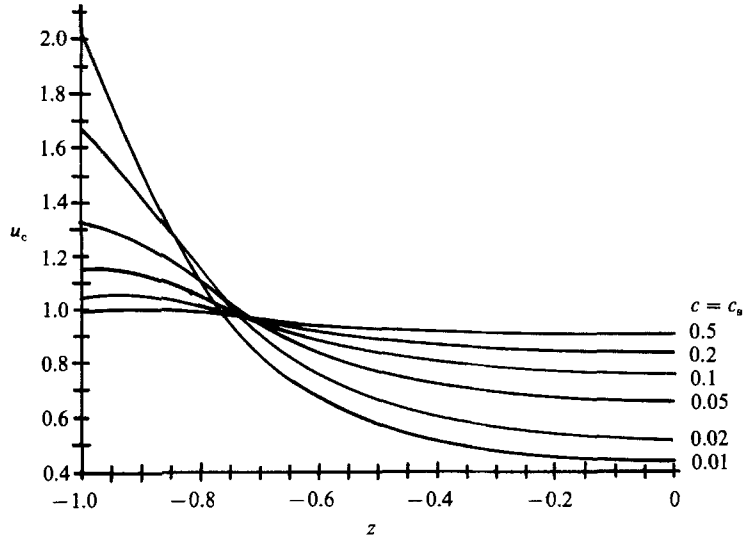

FIGURE 6. Plots of the core velocity u_c at $x = -1$ and at $y = f_b$ for $a = 1$ and for $c = c_s = 0.01$, 0.02, 0.05, 0.1, 0.2, and 0.5.

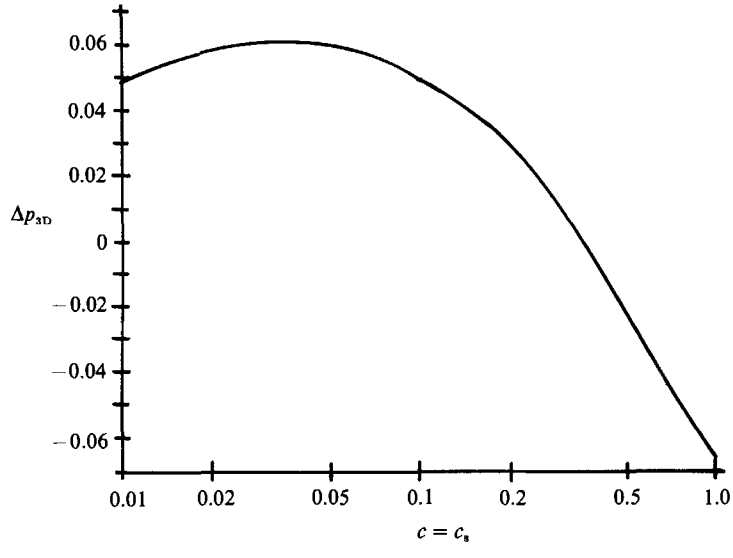

FIGURE 7. Three-dimensional pressure drop for $a = 1$ and equal values of c and c_s. Actual pressure drop equals Δp_{3D} plus the reference pressure drop given by the upstream and downstream fully developed pressure gradients for $x < \frac{1}{2}x_0$ and $x > \frac{1}{2}x_0$, respectively.

the elbow is important for design calculations. A reference pressure drop between any two points far upstream and downstream of the elbow is defined as the pressure drop resulting from the upstream and downstream fully developed flow pressure gradients for $x < \frac{1}{2}x_0$ and for $x > \frac{1}{2}x_0$, respectively. The three-dimensional pressure drop, Δp_{3D}, is defined as the difference between the actual and reference pressure drops between the same two points far upstream and downstream. For $a = 1$ and equal values of c and c_s, Δp_{3D} is plotted in figure 7. For $c = c_s > 0.35$, $\Delta p_{3D} < 0$, which means that the reference pressure drop is larger than the actual pressure drop. Our reference pressure

drop is convenient to compute, but it does not represent the pressure drop for locally fully developed flow. Locally fully developed flow is difficult to define in sector 2 because the boundary-value problem (equations (9), (10), (12), (14), (15)) for sector 2 does not admit solutions with $\partial\phi/\partial x = 0$ and $\partial^2 p_c/\partial x^2 = 0$. We might define the locally fully developed pressure gradient at each cross-section of sector 2 as the fully developed pressure gradient for a duct with the local vertical height $(f_t - f_b)$ and with parallel top and bottom at $\theta = \frac{1}{2}(\theta_u + \theta_d)$. However, this definition leads to an expression which must be integrated numerically in order to obtain the locally fully developed pressure drop through sector 2. For computational convenience, our reference pressure drop uses the average of the upstream and downstream fully developed pressure gradients for sector 2. The locally fully developed gradient defined above decreases very rapidly as x increases from x_0, so it gives a smaller pressure drop than the reference pressure drop. The graph of Δp_{3D} has a maximum of 0.06 at $c = c_s = 0.05$. The asymptotic solution for $c \ll 1$ predicts that Δp_{3D} is proportional to $c^{\frac{1}{3}}$ (Walker 1981), so that Δp_{3D} should increase as c increases. This variation is clearly not valid for any c considered here, which confirms the statement that the small c asymptotic solution is not valid for $c \geqslant 0.01$. For very large c, the flow is nearly locally fully developed, corresponding to some negative Δp_{3D} with our reference pressure. Therefore Δp_{3D} must always have a maximum between the flow with very thin walls which make all pressure variations small and the flow with thick walls which make the flow locally fully developed.

6. Conclusions

The present predictions for the three-dimensional flow distribution differ dramatically from the previous predictions mentioned in §1. Hunt's order-of-magnitude argument (cited by Holroyd 1980) treats the sharp elbow with $\theta_u = 0$ and $\theta_d = 90°$, i.e. with perfect alignment between the downstream duct's centreline and the magnetic field. Hunt's argument predicts that all the flow in the downstream duct is concentrated in a boundary layer with $O(N^{-\frac{1}{3}})$ thickness, adjacent to the top which is located at $x = -a$ for $\theta_d = 90°$. The flow for $-a < x < 0$ is virtually stagnant, and the $N^{-\frac{1}{3}}$ layer spreads very gradually as we move along the downstream duct away from the elbow. The present analysis for $\theta_d = 84.29°$ shows that there are no stagnant regions, even for $c = c_s = 0.01$, and that the flow is actually concentrated slightly more near the bottom than the top in sector 2. The results would not be radically different for values of θ_d closer to 90°. Hunt's argument assumes that the electric currents are small because they must flow through the thin metal walls and that the flow cannot cross the magnetic field lines in the downstream duct if the electric currents are small. These assumptions are based on the small c asymptotic solutions presented by Holroyd & Walker (1978). Based on the present arbitrary c solutions, we conclude that the thin metal walls permit significant electric current circulations, even for $c = c_s = 0.01$, and that these currents allow the flow to cross the magnetic field lines in the radical expansion of sector 2. Hunt's prediction that Δp_{3D} is proportional to $N^{-\frac{1}{3}}$ provides values which are not radically different from the values presented in figure 7, but it neglects the strong dependence of Δp_{3D} on c and c_s. Hunt's argument involves a balance between the EM body force and the inertial 'force', while we neglect the inertial effects in the core regions because $N \gg 1$. Our results show that accelerations are not particularly large at any point in any of the three core regions, so that inertial effects are probably negligible in the cores for $N = 10^4 - 10^5$. Inertial effects may be important in the high-velocity side layers or in

the high-acceleration interior layers, but this analysis is still valid if c and c_s are larger than δ, the layer thickness. For $N = 10^5$, $\delta = N^{-\frac{1}{3}} = 0.022$, which is not smaller than some values of c and c_s considered here. In our analysis, the electric current from the top or bottom must enter the side at $z = -1$ and must flow down or up the side until it passes through the side layer to the core as a uniform j_z. For small c and c_s, a significant fraction of the current from the top or bottom enters the side layer directly and then flows into the core, completely bypassing the side. Therefore, the side layer is an electrical conductor in parallel with the side. The side layer permits more current circulation which increases the pressure drop, but also reduces the severity of the three-dimensional disturbance. It may be possible to model the role of the side layer in the electrical circuit by using an effective c_s. Such an approximation requires a model for side layers with significant inertial effects and such a model does not exist at present.

Moon & Walker (1988) treat the flow in a gradual elbow with a radius of curvature which is much larger than the cross-sectional dimensions of the duct. If this model is extrapolated to a small radius of curvature, it predicts that the flow in the elbow (corresponding roughly to sector 2) is concentrated in thin boundary layers adjacent to the sides, while the fluid for $-1 < z < 1$ is virtually stagnant. In this large-radius asymptotic solution, the electric current densities in the walls are much smaller than j_x and j_y in the liquid metal, so that the axial currents are trapped in the liquid metal for the very long distances required to bleed through the thin walls. This asymptotic solution is appropriate for large-radius elbows because the required long distances are an intrinsic feature of the geometry. However for sharp elbows, large potential gradients drive larger currents in the walls, and the three-dimensional electric current circulation can complete its circuit in axial lengths which are much shorter than those predicted by the extrapolation of the analysis of Moon & Walker (1988). The large-radius solution predicts a Δp_{3D} which is again proportional to $c^{\frac{1}{2}}$. Extrapolated to small radii, this prediction overestimates Δp_{3D}, particularly for larger values of c and c_s, and it misses the fact that Δp_{3D} has a maximum at $c = c_s = 0.05$ for $a = 1$.

This research was supported by the US Department of Energy through the Fusion Power Program at Argonne National Laboratory.

REFERENCES

HOFFMAN, M. A. & CARLSON, G. A. 1971 Calculation techniques for estimating the pressure losses for conducting fluid flows in magnetic fields. *Lawrence Radiation Laboratory Rep.* UCRL-51010, Livermore, California.

HOLROYD, R. J. 1980 An experimental study of the effects of wall conductivity, non-uniform magnetic field and variable area ducts on liquid metal flows at high Hartmann number. Part 2. Ducts with conducting walls. *J. Fluid Mech.* **96**, 355.

HOLROYD, R. J. & MITCHELL, J. T. D. 1982 Liquid lithium as a coolant for Tokamak fusion reactors. *Culham Laboratory Rep.* CLM-R231, Abingdon, Oxfordshire.

HOLROYD, R. J. & WALKER, J. S. 1978 A theoretical study of the effects of wall conductivity, non-uniform magnetic field and variable-area ducts on liquid-metal flows at high Hartmann number. *J. Fluid Mech.* **84**, 471.

HUA, T. Q., WALKER, J. S., PICOLOGLOU, B. F. & REED, C. B. 1988 Three-dimensional magnetohydrodynamic flows in rectangular ducts of liquid-metal-cooled blankets. *Fusion Technology* **14**, 1389.

HUNT, J. C. R. 1965 Magnetohydrodynamic flow in rectangular ducts. *J. Fluid Mech.* **21**, 577.

HUNT, J. C. R. & HOLROYD, R. J. 1977 Applications of laboratory and theoretical MHD duct flow studies in fusion reactor technology. Culham Laboratory Report CLM-R169, Abingdon, Oxfordshire.

HUNT, J. C. R. & LEIBOVICH, S. 1967 Magnetohydrodynamic flow in channels of variable cross section with strong transverse magnetic fields. *J. Fluid Mech.* **28**, 241.

MALANG, S. *et al.* 1988 Self-cooled liquid-metal blanket concept. *Fusion Technol.* **14**, 1343.

MOON, T. J. 1989 Liquid metal flow in a sharp elbow in a uniform transverse magnetic field. PhD dissertation, University of Illinois at Urbana-Champaign.

MOON, T. J. & WALKER, J. S. 1988 Liquid metal flow in a large-radius elbow with a uniform magnetic field. *J. Méc.* **7**, 443.

PICOLOGLOU, B. F., REED, C. B., DAUZVARDIS, P. V. & WALKER, J. S. 1986 Experimental and analytical investigation of magnetohydrodynamic flow near the entrance of a strong magnetic field. *Fusion Technol.* **10**, 860.

REED, C. B., PICOLOGLOU, B. F., HUA, T. Q. & WALKER, J. S. 1987 ALEX results – a comparison of measurements from a round and a rectangular duct with 3-D code predictions. *Proc. IEEE 12th Symp. on Fusion Engng* **2**, 1267.

SHERCLIFF, J. A. 1956 The flow of conducting fluids in circular pipes under transverse magnetic fields. *J. Fluid Mech.* **1**, 644.

SMITH, D. L. *et al.* 1985 Blanket comparison and selection study. *Fusion Technol.* **8**, 1.

TALMAGE, G. & WALKER, J. S. 1988 Three-dimensional laminar MHD flow in ducts with thin metal walls and strong magnetic fields. Liquid metal flows: magnetohydrodynamics and applications. *Prog. Astro. Aero.* **111**, 3.

WALKER, J. S. 1981 Magnetohydrodynamic flows in rectangular ducts with thin conducting walls. Part 1. Constant-area and variable-area ducts with strong uniform magnetic fields. *J. Méc.* **20**, 79.

WALKER, J. S., LUDFORD, G. S. S. & HUNT, J. C. R. 1972 Three-dimensional MHD duct flows with strong transverse magnetic fields. Part 3. Variable-area rectangular ducts with insulating walls. *J. Fluid Mech.* **56**, 121.